

# U-Net based particle localization in granular experiments: Accuracy limits and optimization

Fahad Puthalath<sup>1,2\*</sup>, Matthias Schröter<sup>3\*</sup>, Nicoletta Sanvitale<sup>1,4</sup>,  
Matthias Sperl<sup>1,2</sup>, Peidong Yu<sup>1\*</sup>

<sup>1\*</sup>Institut für Frontier Materials auf der Erde und im Weltraum, Deutsches Zentrum für Luft- und Raumfahrt (DLR), Köln, 51170, Germany.

<sup>2</sup>Institut für Theoretische Physik, Universität zu Köln, Zùlpicher Strasse 77, Köln, 50937, Germany.

<sup>3</sup>Institute for the Dynamics of Complex Systems, University of Göttingen, Friedrich-Hund-Platz 1, Göttingen, 37077, Germany.

<sup>4</sup>Istituto di Radio Astronomia, INAF, Via P. Gobetti 101, Bologna, 40129, Italy.

\*Corresponding author(s). E-mail(s): [fahad.puthalath@dlr.de](mailto:fahad.puthalath@dlr.de);  
[matthias.schroeter@phys.uni-goettingen.de](mailto:matthias.schroeter@phys.uni-goettingen.de); [peidong.yu@dlr.de](mailto:peidong.yu@dlr.de);

## Abstract

Identifying the positions of granular particles from experimental images is often complicated by their partial overlap in two dimensional projections. Uneven backgrounds and inhomogeneous illuminations can add to the challenge. Conventional image-processing methods are often unable to analyze such images. We show that a deep neural network with an U-Net architecture can provide precise particle positions with a high detection rate. For our challenging test image the network correctly identifies 97.7% of the particles while only creating 2.7 % of false positives. The training of the U-Net requires a number of target images where the position of all particles have been identified by humans. Those positions are then indicated in the target images by setting a small number of mask pixels to white in an otherwise black image. We demonstrate that the design of these masks critically determines performance: mask size controls the resolution of overlapping particles, anti-aliased masks enable subpixel accuracy, and systematic human labeling biases set a measurable lower bound on achievable precision. Our final network achieves an accuracy of the particle coordinate of 3.7% of the particle diameter.

**Keywords:** U-Net, particle tracking, instance segmentation

## 1 Introduction

Experimental investigations of granular fluids often require particle tracking for the measurement of various statistical quantities, such as the spatial and velocity distributions, the mean squared displacement, the diffusivity, etc. [1–9].

The first step in particle tracking is the identification of the individual particles and a precise determination of their position within the image. The task of identifying all image pixels belonging to the particles is called segmentation and it comes in two flavors: semantic segmentation, which means to simply mark all pixels belonging

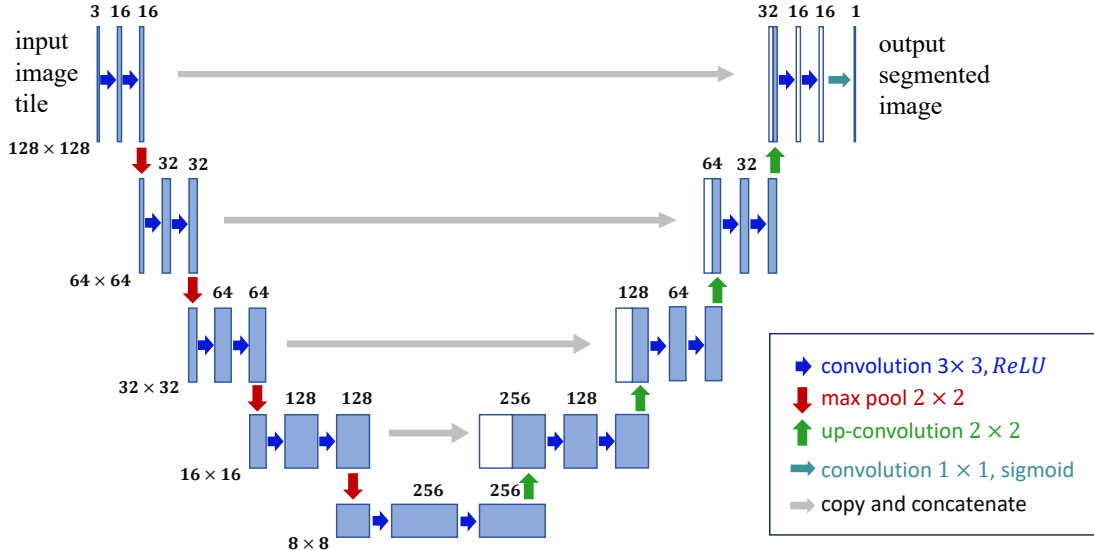


**Fig. 1** The U-Net architecture adopted in our study. The arrows show the flow of information. The *contraction path* (red arrows) and the *expansion path* (green arrows) form a U-shaped information bottleneck that forces the neural network to learn semantic content. Additionally, there are the *copy and concatenation paths* (gray arrows) which preserve the spatial resolution of the original image. The numbers on top of the blocks (and their width) indicate how many feature maps of that size are implemented.

to any of the particles, and instance segmentation, where the pixels belonging to each particle are identified by a different label.

There are two main challenges that the segmentation of granular gas images needs to overcome: first, the three-dimensional nature of the sample results in overlapping particles even in the case of a dilute system. This is particularly problematic for instance segmentation techniques. Second, in order to enable free particle motion, such granular experiments are often performed in low-gravity conditions such as inside a sounding rocket or a drop tower experiment. The illumination conditions in the confined spaces of these setups are often sub-optimal [10] which means that the same particle will appear differently in different regions of the sample container. Classical image processing techniques have difficulties to handle this type of image material, c.f. [11] or Section 2.2. On the other hand, it has been shown that specialized Convolutional Neural Networks (CNNs) can provide excellent segmentation results on complicated images. A good example is their great success in the biomedical sciences [12–16].

The use of CNNs in the detection of granular particles under microgravity has been pioneered by Puzyrev *et al.* [11, 17] who use Mask

R-CNN [18] for tracking rod-shaped granular particles. Mask R-CNN is a two stage algorithm which first identifies a bounding box for each particle and then performs an instance segmentation within that bounding box. A different approach to segmentation is training a generic CNN on multi-resolution image tiles to determine whether the center pixel of the stack is inside or outside the considered objects [19].

Most of the deep learning segmentation pipelines for granular media are based on the U-Net architecture which was initially developed for the segmentation of biomedical images [20]. U-Nets transform input images into output images of the same size that directly represent the segmentation result. Figure 1 shows the characteristic U-shaped architecture that gives the network its name. U-Nets have been used to identify the positions of tracer particles in fluid dynamics experiments [21], the outlines of stress-birefringent disks [22], for the extraction of three-dimensional coordinates from holographic images of particle distributions [23], and for the segmentation of rock fragments [24].

This paper describes the U-Net architecture we employed to locate spherical metal particles inside a spherical container used in a drop tower

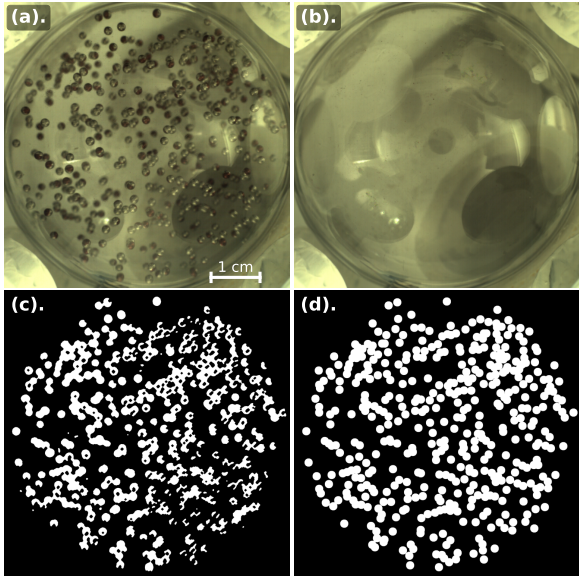


**Fig. 2** Deep learning identifies the particle positions significantly better than classical image processing methods: (a) Raw image from the drop tower experiment. (b) Synthetic background image illustrating inhomogeneous illumination and container reflections. (c) Semantic segmentation (white pixels indicate particles) via classical image processing. (d) Instance segmentation produced by a trained U-Net.

experiment. Section 2 introduces our experimental data and expounds the impossibility to analyze them with classical image processing techniques. Section 3 describes the technical details of our machine learning work-flow. Section 4 discusses important aspects and considerations for preparing the target images used for the training, including the influence of the human labelers. Section 5 describes the influence of different choices of hyper-parameters when training the U-Net. We then close with a summary and conclusion.

This paper is accompanied by the source code of our network, its weights, and the data set used for training, validation, and testing.

## 2 Experimental data and classical image analysis

### 2.1 Experimental setup

The images analyzed in this paper are gathered in an experimental study of granular gases in low gravity. During a typical experiment, approximately 450 spherical magnetic particles of 1.6 mm

in diameter are magnetically shaken in a transparent spherical sample cell of diameter 60 mm. The experiment is conducted in a drop tower in Bremen, Germany, operated by the Center of Applied Space Technology and Micro-gravity (ZARM) of the University of Bremen. In this facility, we can achieve up to 9.3 s of low gravity, with a gravity level less than  $10^{-4}g$  [25]. This allows us to study the behavior of granular gases in a microgravity environment. The particle dynamics is captured using a high speed camera (EoSens 4CXP from Mikrotron GmbH) with 165 fps. The spatial resolution of our setup makes the mean particle diameter  $D$  correspond to 38 pixels.

Fig. 2a shows a raw image from the experiment. Several problems are visible: First, due to space constraints of the magnetic excitation mechanism, the illumination conditions inside the sample cell is inhomogeneous, causing the gray value range of the particle pixels to sometimes overlap with that of the background. In addition, reflections of the surrounding experimental setup are visible on the spherical surface of the sample container. Finally, a fraction of the particles overlap with each other due to the three-dimensional nature of the experiment.

### 2.2 Classical image analysis

Classical image segmentation pipelines typically combine semantic and instance segmentation. The first step is the semantic segmentation where the image is binarized, i.e. each pixel is assigned to either the set of all particles or to the background. Because semantic segmentation is often based on the pixel gray values, illumination conditions play an important role at this stage. The following instance segmentation, where each particle pixels is assigned to an individual particle, becomes an easier task if the relevant pixels have already been identified. However, the apparent overlap between particles, which is unavoidable for three-dimensional experiments, will complicate this step.

Due to the challenging illumination conditions in our experiment, classical image processing fails already at the semantic segmentation stage, as shown in figure 2(c). Because of the inhomogeneous illumination visible in figure 2(b), we could not simply work with one or two global gray value

thresholds to identify the pixels belonging to particles. We therefore evaluated for each pixel how much its gray value deviates from the gray value of the background at that same position. Working with the image color instead of the gray value alone did not yield any improvement.

In order to do so we first generated a synthetic background image by analyzing the gray value statistics of each pixel; Figure 2(b) demonstrates the success in this task. Then, if the gray value of an image pixel is within a certain range around the gray value of the same pixel in the background image, we assume the deviation is noise and classify it as a background pixel. Otherwise, we assign that pixel to the set of particle pixels. Even after some postprocessing with morphological filters, the result in figure 2(c) is unsatisfying as many particles appear incomplete or fragmented.

On the other hand, it is possible for a human observer, making use of geometrical cues and texture information, to identify the actual particles, which suggests that neural networks should be capable of solving this problem. Fig. 2(d) shows that this conclusion is indeed correct and we will explain this method in the following sections.

### 3 Particle detection using an U-Net

#### 3.1 Creating training, validation, and test data

Each machine learning project requires a separation of the available data into training data, validation data for the optimization of the hyper parameters of the model, and test data which provide an independent evaluation of the final model performance. Special care needs to be taken that the test data does not overlap with the training and the validation data since otherwise the performance evaluation would be compromised [26]. During the training of our network, this condition is guaranteed by using separate images for each of the three groups. As shown table 1, of the 28 images for which we have identified the positions of all particles by human observation, we use 20 for training the network, 7 for validation, 1 for and testing.

Data set	Number of Images	Tiles	Particles
Training	20	8820	9025
Validation	7	3087	3109
Testing	1	441	427

**Table 1** Sizes of the data sets used for training, validating, and testing.

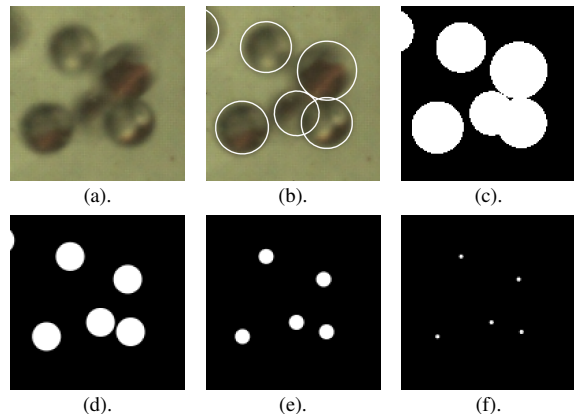


**Fig. 3** Training of the network requires for each tile a mask image (the target) where the particle positions are indicated with white circular masks: (a) Original image tile. (b) Manually drawn circles in imageJ used to determine particle coordinates. (c) Corresponding mask image with mask radius equal to the particle radius. (d)-(f) Mask image with smaller mask radii  $R = 10, 5, \text{ and } 1$  respectively. Smaller masks help to resolve overlapping particles, as discussed in Section 5.1.

The raw images taken by our cameras are  $1380 \times 1380$  pixels in size, too large for an efficient training of our deep learning architecture. Following [22], we cut each image into 41 overlapping tiles of size  $128 \times 128$  pixels (see one such tile in Fig. 3a. Adjacent tiles overlap by 50% of their side length, i.e., by 64 pixels in both horizontal and vertical directions, in order to reduce border artifacts. Given that each spherical particle has an average diameter of  $D \approx 38$  pixels in the images, each tile contains only a few particles. We then manually identify the particle positions in each tile and generate an image tile with masks (see Fig. 3 c-f) and a list of particle centers. This process is discussed in more details in Section 4.2. The full output image is reconstructed by combining the predictions from all tiles while retaining only the central region of each tile to avoid edge effects.

Eventually, 11907 image tiles with size  $128 \times 128$  are prepared for the training and validation (see table 1 for more details).

### 3.2 Network architecture and training

The architecture of a U-Net is described in Fig. 1. It is trained using an image tile as input and a corresponding manually generated mask tile as ground-truth. U-Nets combine two pathways of information flow. The first one is U-shaped and consist itself of two consecutive steps. First the input image is reduced in size in 4 steps from  $128 \times 128$  down to  $8 \times 8$  pixels using max-pooling. At each resolution the image is processed by two consecutive convolution operations combined with an 10 to 30 % dropout in order to avoid overfitting [27]. Then the  $8 \times 8$  feature maps are expanded again to the original size using  $2 \times 2$  up-convolutions. Again, at each size, there are 2 consecutive convolutions with dropout in between. Even though this path partially compensates for the loss of spatial resolution by increasing the number of feature maps from 16 at full resolution to 256 at the  $8 \times 8$  level, the reduction in capacity forces the network to learn the semantic content of the images, quite similar to an autoencoder [28].

The second pathway consists of a group of four skip connections which copy, at each resolution, the feature maps from the contraction path to the expansion path (the gray arrows in Fig. 1). These copies are concatenated with the up-convoluted feature maps so that the subsequent convolutions also have access to the original images at this spatial resolution, which assures a high spatial fidelity of the final result [20].

As described in Section 4.2, the gray value of each pixel in the mask images describes the fraction of its area covered by a circle of desired radius drawn around the center coordinates. This fixes the value range to 0 (completely outside of any particle) to 1 (completely inside). Therefore, a generic implementation for the output layer is a  $1 \times 1$  convolution filter with sigmoid activation function acting on the last 16 feature maps. All other convolution filters use a filter mask of fixed size, between  $3 \times 3$  and  $9 \times 9$ , and Rectified Linear Units (ReLU) as activation functions. The effect of the filter size will be discussed in Section 5.3.

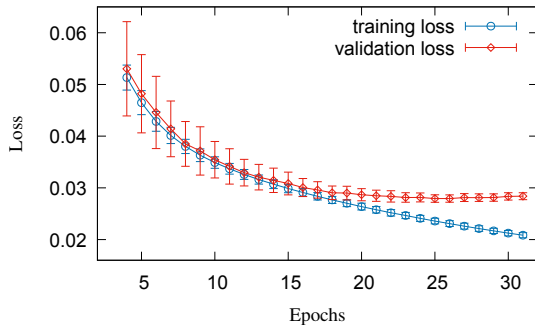


**Fig. 4** During training, the validation loss typically saturates after 30-60 epochs. Data is averaged over 10 different random initializations of the same model.

The network is implemented in TensorFlow using the Keras API. Training is performed with an Adam optimizer and a fixed learning rate of  $10^{-4}$  using binary cross entropy as loss. Given the pronounced imbalance between white and black pixels in our masks, we have also tested focal loss [29] and Dice loss [30]. We find that differences in the quality of the prediction, as discussed in the next chapter, are well within the standard deviation of those measures. We therefore abide with binary cross entropy. Figure 4 shows the evolution of training and validation loss during typical training runs.

The output image of the U-Net is a gray-scale image where each pixel's value indicates the confidence of the network that this pixel belongs to a particle's mask (which is smaller in diameter than the particle itself). In order to identify the particle centers we use four postprocessing steps in *ImageJ* [31]. First, the image is binarized with a cutoff value  $T$ . Section 5.3 discusses this hyperparameter in more detail. Then, the individual particles are identified using the watershed tool [32] which is internally preceded by an Euclidean Distance transform. This steps also resolves any remaining overlaps. The boundaries found by the watershed algorithm are then used to identify each particle as a list of pixels in the original gray value image. Finally, the center of mass of each separate list is determined with the Analyze-Particle tool.

### 3.3 Evaluating the quality of the prediction

There are three different aspects which determine the quality of our image processing. First, there is the question if the U-Net does correctly identify all particles visible in the image and also does not hallucinate additional particles. This becomes especially important if we construct particle trajectories using the positions from a sequence of images (not discussed in this manuscript). Second, we care for the accuracy of the positions of the detected particles. This becomes important for determining their precise velocities. Finally, as discussed in Section 2.2, there is the challenge to resolve partially overlapping particles as two entities.

All three of these properties are measured on the validation data in order to learn their dependence on the choice of hyperparameters. Additionally, they are determined relative to the results of human labeling; we do not have access to an independent ground truth. Here, we first introduce the appropriate measures, the dependency on the hyperparameters will be discussed in Section 5, the dependence on the human labeler in Section 4.3.

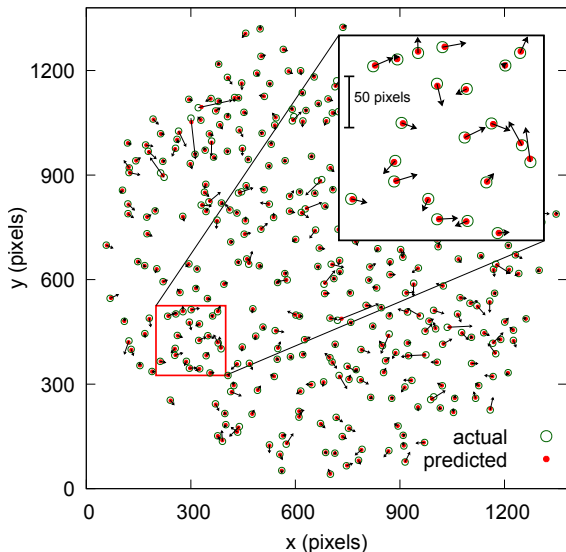


**Fig. 5** Vectors  $\vec{s}$  illustrating the discrepancy between manually identified particle positions (green rings) and the positions determined from the U-Net prediction (red dots). The length  $s$  of each vector is magnified 10 times for visibility.

For the decision whether a predicted particle position is correct or hallucinated, we find for each predicted particle the nearest particle position in the manually labeled target image. This pair defines a separation vector  $\vec{s}$ , see Fig. 5 for an illustration.

A particle is considered to be correctly found, or *True Positive (TP)*, if  $|\vec{s}| \leq 20$  pixels. This threshold correspond to about half a particle diameter. If a predicted particle has no partner in the labeled image with  $|\vec{s}| \leq 20$  pixels, we consider it a hallucination or *False Positive (FP)*. Finally, there are *False Negatives (FN)*, i.e. manually labeled particles that have no predicted counterpart in a radius smaller than 20 pixels.

Using these three labels, we can compute two quality metrics: the *precision*,  $p = TP/(TP+FP)$  and the *recall*,  $r = TP/(TP+FN)$  where we would aim for both to be as close to 1 as possible. However, we decided to optimize the hyperparameters of our U-Net using a combined measure, the  $F_\beta$  score defined as

$$F_\beta = \frac{(1 + \beta^2) \cdot TP}{(1 + \beta^2) \cdot TP + FP + \beta^2 \cdot FN}$$

By choosing  $\beta = 2$ , we give a higher weight to *recall* and thus to minimizing *FN*. This decision is motivated by our aim to subsequently reconstruct the three-dimensional trajectories of the particles. The necessary algorithms are not symmetric with regard to the presence of *FN* and *FP*: while a *FN* particle will split a trajectory into two shorter parts, a *FP* particle will typically be ignored due to the absence of possible predecessor or successor particles in the time series.

In order to measure the ability of the network to identify partially overlapping particles, we measure the percentage of particle pairs that are correctly detected as two separate centers rather than a single merged detection. This percentage is a function of the separation distance between the two particle centers; its dependence on mask size will be discussed in Section 5.1.

Finally, the separation vector  $\vec{s}$  is also used directly to quantify the quality of the predictions: optimally it would be as small as possible for all particles in the validation dataset. Additionally, any measurable deviation from an isotropic angular distribution points to a systematic error.

## 4 Creating mask images for training

The U-Net results can only be as good as the image and mask pairs it has been trained with. Therefore, the preparation of high quality masks is paramount. Creating mask images requires two consecutive steps: First a human labeler has to create a list of the particle centers, then the binary mask image has to be created by drawing filled white circles at those positions into an otherwise black image. In Sections 4.1 and 4.2 we will discuss some caveats regarding these two steps. Section 4.3 describes how different human labeler have different biases and how an ensemble of labelers can be used to finetune the model.

### 4.1 Identifying particle centers

While there are other open source solutions for labeling training data [33], we found the image processing program *ImageJ* [31] most suitable for this task. After the image is loaded, the human labeler can zoom into the image as desired and draw circles around the identifiable particles, as shown in Fig. 3b. *ImageJ* processes this information and outputs a list of the particle centers as floating point values. A set of instructions for training prospective labeler is included in the supplemental material.

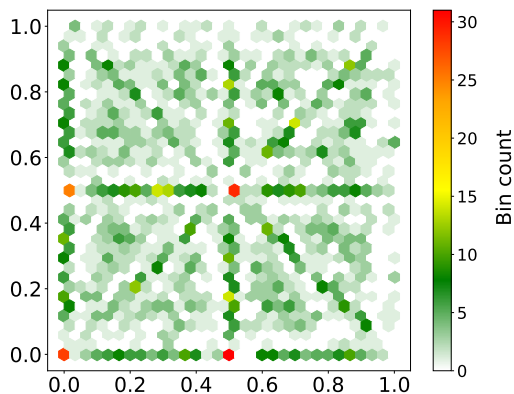


**Fig. 6** The distribution of decimal places in the particle coordinates reported by *ImageJ* is not uniform. The color bar shows the frequency of coordinate pairs falling in each hexagonal bin, which reveals a bias towards integer or half-integer values. The data is generated from 2157 particle coordinates obtained from 5 images.

During the labeling of our images we found that *ImageJ* has a minor issue. One would expect the decimal places of the particle coordinates to be uniformly distributed between 0 and 1 in both the  $x$  and  $y$  directions. However, as shown in Figure 6, this is not the case: the likelihood of obtaining an integer or a half-integer value is significantly higher than the average. This behavior can be traced back to a form of ‘snapping’ of the coordinate values; it can be reproduced by drawing slightly shifted circles at a high magnification. Based on the insight that the imperfections of the human labelers (discussed in section 4.3) are larger than the error created by *ImageJ*, we decided to accept this limitation.

### 4.2 Making binary mask images

The second step in the creation of the mask images is to use the particle coordinates to draw filled white circles of radius  $R$  in an otherwise black image. Figure 3 (d) to (f) gives an example. The choice of  $R$  is an important hyperparameter; its influence on the results is discussed in Section 5.1.

A naive way of doing so would be to round the particle coordinates to the next integer value and use the corresponding pixel as the center of the circle to be drawn. However, this would introduce a systematic error due to the difference between the actual pixel center and the coordinates used to address it. For example, let us assume our center coordinates are  $x = 12.4$  and  $y = 12.6$ . If our mask had the size of only one pixel, we should choose the pixel indexed (12,12) which has a center of 12.5, 12.5 in the global coordinate system used to measure particle centers. However, rounding to the next integer results in the pixel indexed (12,13) being chosen as the center.

The correct way of turning the floating point numbers into integers is therefore the floor operation, because it assures that all decimal values between 0.000... and 0.9999... get mapped onto the integer below, which then creates a particle center at 0.5. This point is also proven numerically in figure 7 (a).

A second, more subtle issue of integer based mask centers arises from the uneven distribution shown in figure 6. The red-colored maxima at  $x$  and/or  $y$  equals zero show that real centers in some unknown range around zero will snap to exactly zero as decimal place. For centers located

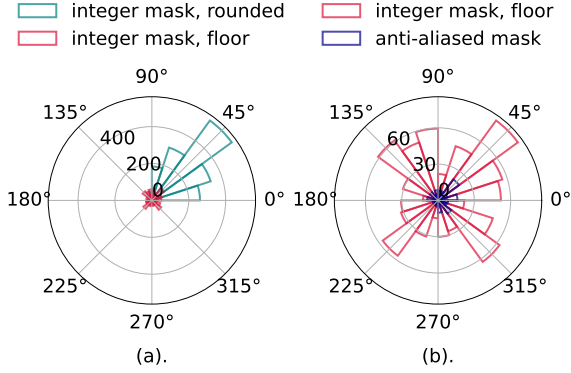


**Fig. 7** A tool to study systematic bias are polar histograms of displacement vectors between particle centers obtained during manual labeling and those extracted from the corresponding mask images. The vectors are grouped into 20 angular bins of  $18^\circ$  each, and the radial value indicates the sum of vector magnitudes within each bin. Histograms are computed from 2157 particle coordinates. (a) Integer mask centers obtained by rounding introduce a systematic bias, whereas using the floor operation removes this effect. (b) Anti-aliased, floating-point-based masks further reduce the positional error. For visibility, the displacement magnitudes of anti-aliased masks in (b) are scaled by a factor of ten.

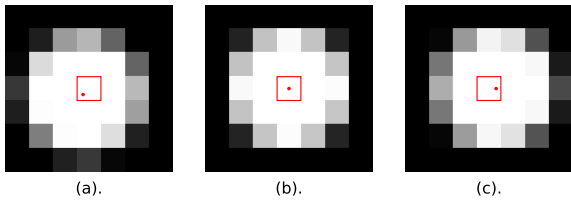


**Fig. 8** Anti-aliased masks can be centered around floating point positions (the red dots). Shown are masks with a radius of 2 pixels centered at (a)  $x = 3.25, y = 3.25$ , (b) at  $x = 3.50, y = 3.50$  and (c) at  $x = 3.80, y = 3.50$ . The red square indicates the integer center of the masks which is identical in all three cases.

slightly left and/or below those red points, this results in an erroneous increase of the center position by one pixel. For example, a real particles center of 11.98 which would be reported as 12 by ImageJ, leading to a mask center of 12.5 instead of 11.5 [34].

#### 4.2.1 Anti-aliased masks

The best way to avoid all the problems associated with an integer based center position of the particle masks is to use anti-aliased masks which can be positioned with floating point accuracy.

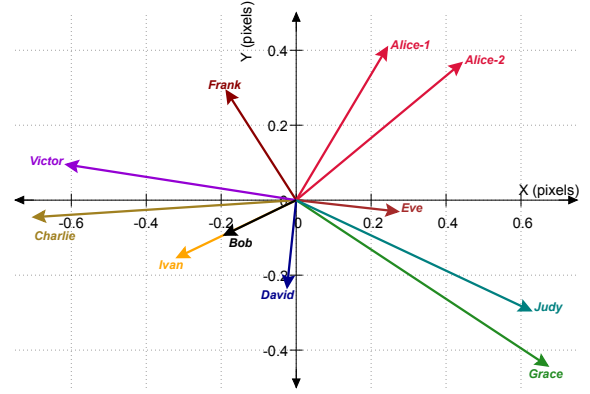


**Fig. 9** Human labeler exhibit a systematic bias in their annotations. Each vector represents the mean deviation of a labeler's coordinates from the consensus (mean) positions. Data was gathered from one test and one training image.

To create these masks, an imaginary circle of the intended radius is overlaid over a grid of square pixels. All pixels which are completely within the circle are set to white. Pixels that are cut into two by the circle are colored with a gray value which is proportional to the pixel area within the circle. Figure 8 gives an example how these anti-aliased masks change with the exact position of the mask center. Figure 7 (b) depicts the clear superiority of these anti-aliased masks over the integer based ones.

### 4.3 The influence of the human labeler

To investigate the influence of human labeler on the ground truth coordinates, we conducted an experiment where multiple people were asked to manually annotate the same images. The coordinates obtained from each labeler were then grouped using the DBSCAN algorithm [35] to identify particles that were consistently labeled by all participants. For each particle, we calculated the mean coordinate and the separation of each labeler's coordinate from this mean position. By averaging these separations across all particles identified by each labeler, we obtained a mean separation vector for each labeler.

The results, plotted in Fig. 9, show that the mean separation vectors for each labeler point in different directions, indicating the systematic bias for each labeler. Notably, the vectors for labeler "Alice", who annotated two images, both lie in

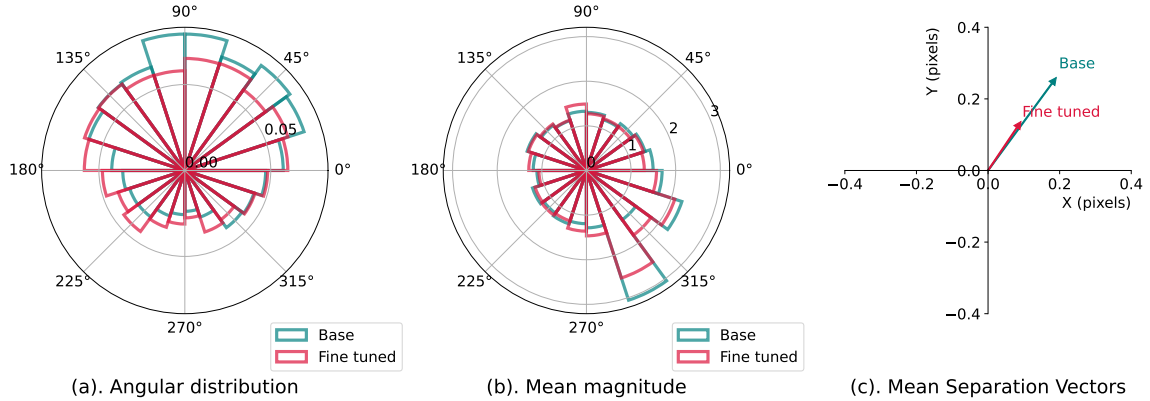


**Fig. 10** Fine-tuning the model using as ground truth the mean coordinates of multiple labelers reduces the bias. These graphs are based on the displacement vectors  $\vec{s}$  for a test image that has been labeled by 6 people (Alice, Bob, Eve, Victor, Ivan, Judy). The base model (teal line) has been trained with images only analyzed by Alice and Bob. After the base model has been fine tuned with a training image analyzed by 5 people (Alice, David, Charlie, Frank, Grace) it produced the results shown in red. (a) the angular probability distribution of vectors  $\vec{s}$  becomes more homogeneous after fine-tuning. (b) average length of  $\vec{s}$  as a function of direction. (c) The total bias can be characterized by the mean displacement vector which is computed by averaging  $\vec{s}$  over all directions (this corresponds to the average over a bin-wise multiplication of (a) and (b)).

the first quadrant, providing evidence for the consistency of these biases. The magnitudes of these vectors are relatively small, ranging from 0.20 to 0.60 pixels in both x and y components, suggesting that while the biases are real, they are also relatively subtle.

By acknowledging and accounting for these biases, we can develop a more robust and reliable image segmentation algorithm. The initial training of our model used ground truth data generated by only two labelers (Alice analyzed 13 training images, Bob analyzed 7). However, after collecting additional labels from multiple labelers, we fine-tuned the model by retraining it using as ground truth data the mean positions (in one training image) averaged over the results of 5 different labelers. Figure 10 shows that this fine-tuning decreased the spatial bias of the network. However, the accuracy, measured as the average over all  $|\vec{s}|$ , remains constant at 1.4 pixels corresponding to 3.7% of the particle diameter. This suggests that we are approaching the maximal accuracy achievable with the present data and network architecture.

We anticipate that further improvements can be achieved by increasing the number of labelers and training the network on their mean coordinates. Our results also show that the network is sensitive to training biases which need to be considered when all the training data are created by a single person.

## 5 Optimizing the hyperparameters

As discussed in Section 3.3, we want to optimize three different metrics with our algorithm: the  $F_2$  score for minimizing the False Positives and False Negatives, the mean separation vector  $\vec{s}$  for minimizing the difference between predicted position and ground truth, and the percentage of correctly identified overlapping sphere pairs which we want to maximize. The most important hyperparameters to reach this objective are the radius of our masks  $R$ , the threshold  $T$  used for binarizing the prediction of our U-Net and the filter size  $f$  used in the convolutions

### 5.1 Optimizing the detection of overlapping particles

As discussed in Section 2.2, partially overlapping particles pose a challenge for any segmentation algorithm. It is intuitive that the U-Net has a better chance of distinguishing them when the masks representing the two particles do not overlap. (Note that even if two particles in the output overlap, the watershed step described in Section 3.2 still allow us to separate them.)

This implies that the radius of the masks  $R$  should be significantly smaller than half the particle diameter  $D/2$ , i.e. smaller than 19 pixels for our images. Fig. 11 shows the capability of U-Nets

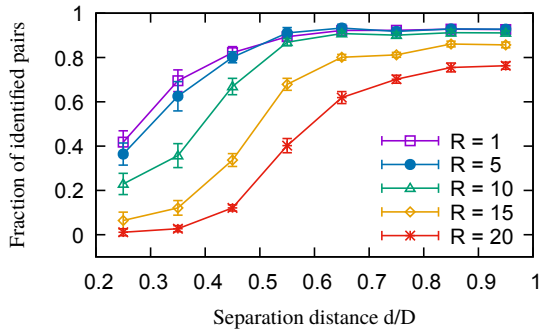


**Fig. 11** The fraction of correctly identified pairs of particles improves with decreasing mask size  $R$  for separation distances  $d$  that are smaller than the particle diameter  $D$  of 38 pixels. Data is averaged over 7 validation images, with 10 different network initializations used to generate the error bars. All measurements are done with  $T$  values maximizing the  $F_2$  and  $f=3$ .

trained with different mask sizes to handle overlapping particles. It can be seen that  $R$  values smaller than 5 do not result in an improvement. As shown below,  $R$  influences also our other target metrics which therefore also have to be taken into account when choosing an optimal value.

## 5.2 Minimizing the mean positional error $\vec{s}$

Given that the anti-aliased masks we use for training (c.f. figure 8) cover at their boundaries the full range of gray values, it is unsurprising that the predicted particle positions are also not binary images. However, as figure 12 (b) shows, the gray value boundaries of the predicted particles extend over a larger range of radii. In order to obtain a precise location we therefore binarize the predicted images with a threshold  $T$  as described in Section 3.2. Since the mean output shown in figure 12 (b) is symmetric, we can expect  $T$  to not influence the size or direction of the individual  $\vec{s}$  vectors. In contrast, the mask radius and the convolutional filter size do have a weak influence as shown in the top part of figure 13. For  $R = 5$  and  $f = 3$  we obtain a mean positional error of 1.9 pixels, or approximately 5% of the particle diameter.

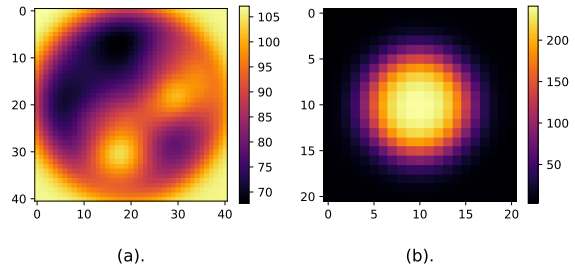


**Fig. 12** Even though the particle images are irregular, the U-Net learns to represent the particles as radially symmetric. (a) Knowing the particle centers, we can average the individual particles images. The result demonstrates the inhomogeneous illumination of our sample. (b) the average over the predicted outputs (here with  $R = 5$  pixels) shows no asymmetry.

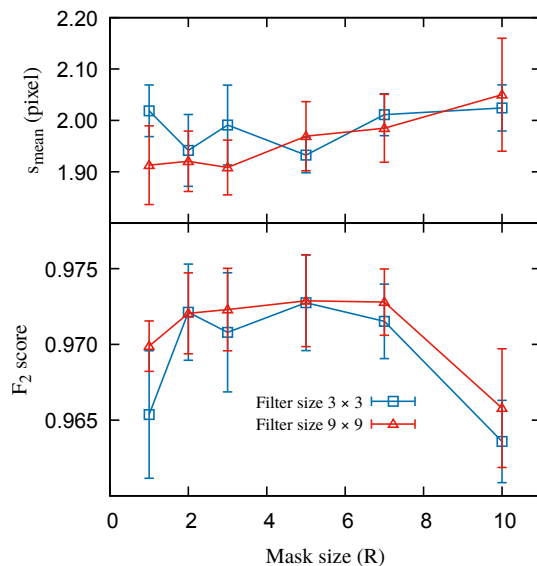


**Fig. 13** Given the size of the uncertainty bars, a mask radius  $R = 5$  and a filter size  $f = 3$  are good choices to maximize the  $F_2$  score and at the same time achieve a small mean separation  $s_{mean}$ . Data is obtained by averaging the results from 10 models trained with different random initializations and evaluated on 7 validation images.  $T$  values were chosen to optimize the  $F_2$  score. Uncertainty bars are standard deviations.

## 5.3 Maximizing the $F_2$ score

The cut-off threshold  $T$  determines which part of the U-Net output is included in the analysis. Setting it too low will discard particles which did not create a strong output signal, setting it too high will merge the gray value clouds of neighboring

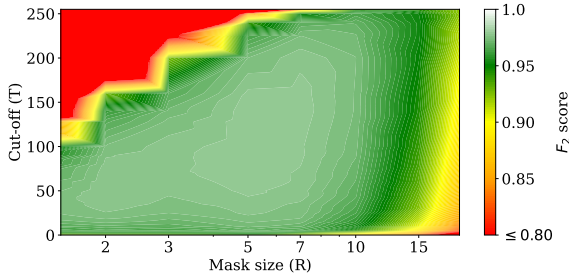


**Fig. 14** For all values of  $R$  there is intermediate value of the cut-off  $T$  which maximizes the  $F_2$  score. All results were obtained with a convolution filter size of 3.

particles. Fig. 14 shows how  $T$  and  $R$  influence the  $F_2$  score. For  $R = 5$  we obtain a broad maximum, allowing us to optimize all three of our metrics at the same time. The bottom part of Fig. 13 shows that this maximum is also not depending on  $f$ .

## 5.4 Final results based on test image

Using a test image where the coordinates have been averaged over 6 labelers we find our fine-tuned (see Section 4.3) U-net has an  $F_2$  score of 0.976. This corresponds to correctly identifying 97.7 % of the particles while only creating 2.7 % of false positives (we assume a particle to be present if it was found by at least two labelers). The mean accuracy of the particle coordinates is 3.7 % of their diameter.

## 6 Conclusion

We have shown that even challenging images of granular experiments can be successfully segmented using a U-Net architecture. We also demonstrated how paying attention to the details in the generation of the training data, including the biases introduced by human labelers, is important to assure optimal results. The optimized U-Net will provide the basis of our future particle tracking work.

The relative insensitivity of our results to the hyperparameters indicates that all information contained in the images has been successfully extracted. A way of proving that point would be a comparison with alternative deep-learning based segmentation algorithms. As we provide both our trained model and the training, validation, and test data under an open source license, this work could serve as a benchmark.

**Acknowledgments.** We thank the following labelers: Kai Albert, Dorian Feisel, Sophia Grille, Sofie Hübl, Sibylle Nägle, Nisha Singh, and Golo Zimmermann. We thank Dmitry Puzyrev, Karsten Tell, and the AIMS team for helpful discussions. The authors gratefully acknowledge the computational and data resources provided through the joint high-performance data analytics (HPDA) project “terabyte” of the German Aerospace Center (DLR) and the Leibniz Supercomputing Center (LRZ).

## Declarations

**Funding** We acknowledge partial funding support from DLR through Project No. 50WK2270D (Artificial Intelligence for Granular Experiments, AIGE, a sub-project of Artificial Intelligence Meets Space, AIMS). Fahad Puthalath is supported by Hanns-Seidel-Stiftung (HSS) and by German Academic Exchange Service (DAAD).

**Conflict of interest** The authors declare no Conflict of interest.

**Code availability** The code of the U-Net, the weights, all training, validation, and test images including labels, and instructions for aspiring labelers will be published on GitHub under CC BY-SA 4.0 license [36].

## References

- [1] Falcon, E., Wunenburger, R., Évesque, P., Fauve, S., Chabot, C., Garrabos, Y., Beysens, D.: Cluster formation in a granular medium fluidized by vibrations in low gravity. *Phys. Rev. Lett.* **83**, 440–443 (1999) <https://doi.org/10.1103/PhysRevLett.83.440>
- [2] Sack, A., Heckel, M., Kollmer, J.E., Zimmer, F., Pöschel, T.: Energy dissipation in driven granular matter in the absence of gravity. *Phys. Rev. Lett.* **111**, 018001 (2013) <https://doi.org/10.1103/PhysRevLett.111.018001>
- [3] Falcon, E., Bacri, J.-C., Laroche, C.: Equation of state of a granular gas homogeneously driven by particle rotations. *EPL (Europhysics Letters)* **103**, 64004 (2013) <https://doi.org/10.1209/0295-5075/103/64004>

- [4] Harth, K., Trittel, T., Wegner, S., Stannarius, R.: Free cooling of a granular gas of rod-like particles in microgravity. *Phys. Rev. Lett.* **120**, 214301 (2018) <https://doi.org/10.1103/PhysRevLett.120.214301>
- [5] Yu, P., Schröter, M., Sperl, M.: Velocity distribution of a homogeneously cooling granular gas. *Phys. Rev. Lett.* **124**, 208007 (2020) <https://doi.org/10.1103/PhysRevLett.124.208007>
- [6] Schneider, N., Musiolik, G., Kollmer, J.E., Steinpilz, T., Kruss, M., Jungmann, F., Demirci, T., Teiser, J., Wurm, G.: Experimental study of clusters in dense granular gas and implications for the particle stopping time in protoplanetary disks. *Icarus* **360**, 114307 (2021) <https://doi.org/10.1016/j.icarus.2021.114307>
- [7] Pitikaris, S., Bartz, P., Yu, P., Cristoforetti, S., Sperl, M.: Granular cooling of ellipsoidal particles in microgravity. *npj Microgravity* **8**(1), 11 (2022) <https://doi.org/10.1038/s41526-022-00196-6>
- [8] Puzyrev, D., Trittel, T., Harth, K., Stannarius, R.: Cooling of a granular gas mixture in microgravity. *npj Microgravity* **10**, 36 (2024) <https://doi.org/10.1038/s41526-024-00369-5>
- [9] Cheng, K., Hou, M., Sun, W., Qiao, Z., Li, X., Lai, C., Yuan, J., Li, T., Ye, F., Chen, K., Yang, M.: Unraveling the role of gravity in shaping intruder dynamics within vibrated granular media. *Communications Physics* **7**, 425 (2024) <https://doi.org/10.1038/s42005-024-01927-9>
- [10] Yu, P., Stärk, E., Blochberger, G., Kaplik, M., Offermann, M., Tran, D., Adachi, M., Sperl, M.: Magnetically excited granular matter in low gravity. *Review of Scientific Instruments* **90**(5), 054501 (2019) <https://doi.org/10.1063/1.5085319>
- [11] Puzyrev, D., Harth, K., Trittel, T., Stannarius, R.: Machine learning for 3d particle tracking in granular gases. *Microgravity Science and Technology* **32**, 897–906 (2020) <https://doi.org/10.1007/s12217-020-09800-4>
- [12] Newby, J.M., Schaefer, A.M., Lee, P.T., Forrest, M.G., Lai, S.K.: Convolutional neural networks automate detection for tracking of submicron-scale particles in 2d and 3D. *Proceedings of the National Academy of Sciences* **115**, 9026–9031 (2018) <https://doi.org/10.1073/pnas.1804420115>
- [13] Midtvedt, B., Helgadottir, S., Argun, A., Pineda, J., Midtvedt, D., Volpe, G.: Quantitative digital microscopy with deep learning. *Applied Physics Reviews* **8** (2021) <https://doi.org/10.1063/5.0034891> . 011310
- [14] Stringer, C., Wang, T., Michaelos, M., Pachitariu, M.: Cellpose: a generalist algorithm for cellular segmentation. *Nature Methods* **18**, 100–106 (2021) <https://doi.org/10.1038/s41592-020-01018-x>
- [15] Liu, Z., Zhang, H., Jin, L., Chen, J., Nedzved, A., Ablameyko, S., Ma, Q., Yu, J., Xu, Y.: U-net-based deep learning for tracking and quantitative analysis of intracellular vesicles in time-lapse microscopy images. *Journal of Innovative Optical Health Sciences* **15** (2022) <https://doi.org/10.1142/s1793545822500316>
- [16] Weigert, M., Schmidt, U.: Nuclei instance segmentation and classification in histopathology images with stardist. In: *The IEEE International Symposium on Biomedical Imaging Challenges (ISBIC)* (2022). <https://doi.org/10.1109/ISBIC56247.2022.9854534>
- [17] Niemann, A., Puzyrev, D., Stannarius, R.: ParticleTracking: A GUI and library for particle tracking on stereo camera images. *Journal of Open Source Software* **10**, 5986 (2025) <https://doi.org/10.21105/joss.05986>
- [18] He, K., Gkioxari, G., Dollár, P., Girshick, R.: Mask r-cnn. In: *Proceedings of the IEEE International Conference on Computer Vision*, pp. 2961–2969 (2017)
- [19] Dillavou, S., Hanlan, J.M., Chieco, A.T., Xiao, H., Fulco, S., Turner, K.T., Durian,

- D.J.: Bellybutton: accessible and customizable deep-learning image segmentation. *Scientific Reports* **14**, 14281 (2024) <https://doi.org/10.1038/s41598-024-63906-y>
- [20] Ronneberger, O., Fischer, P., Brox, T.: U-net: Convolutional networks for biomedical image segmentation. In: *Medical Image Computing and Computer-Assisted Intervention—MICCAI 2015: 18th International Conference, Munich, Germany, October 5–9, 2015, Proceedings, Part III* 18, pp. 234–241 (2015). Springer
- [21] Liang, J., Liu, X., Chen, T., Pan, C., Xu, C.: Particle identification in particle tracking velocimetry using two-stage neural networks. *Journal of Industrial and Management Optimization* **19**, 5331–5352 (2023) <https://doi.org/10.3934/jimo.2022175>
- [22] Sanvitale, N., Gheller, C., Bowman, E.: Deep learning assisted particle identification in photoelastic images of granular flows. *Granular Matter* **24**, 65 (2022) <https://doi.org/10.1007/s10035-022-01222-w>
- [23] Shao, S., Mallery, K., Kumar, S.S., Hong, J.: Machine learning holography for 3D particle field imaging. *Optics Express* **28**, 2987–2999 (2020) <https://doi.org/10.1364/OE.379480>
- [24] Yu, J., Meng, L., Ren, S., Song, X., Liang, H., Cao, J., Xue, Y., Zhou, W.: A method for identifying fragmentation of open-pit mining blasting based on a new hybrid convolutional neural network. *Granular Matter* **27**, 62 (2025) <https://doi.org/10.1007/s10035-025-01542-7>
- [25] Cornelius, M.: ZARM Drop Tower Bremen User Manual. ZARM Drop Tower Operation and Service Company, (2023). ZARM Drop Tower Operation and Service Company
- [26] Kapoor, S., Narayanan, A.: Leakage and the Reproducibility Crisis in ML-based Science. *arXiv*. arXiv:2207.07048 [cs, stat] (2022). <https://doi.org/10.48550/arXiv.2207.07048>
- [27] Bhattiprolu, S.: Defining U-net in Python using Keras. [https://github.com/bnsreenu/python\\_for\\_microscopists/blob/master/074-DefiningU-netinPythonusingKeras.py](https://github.com/bnsreenu/python_for_microscopists/blob/master/074-DefiningU-netinPythonusingKeras.py). Last accessed: Jan 31, 2020 (2020)
- [28] Hinton, G.E., Salakhutdinov, R.R.: Reducing the Dimensionality of Data with Neural Networks. *Science* **313**, 504–507 (2006) <https://doi.org/10.1126/science.1127647>
- [29] Lin, T.-Y., Goyal, P., Girshick, R., He, K., Dollár, P.: Focal Loss for Dense Object Detection. *arXiv*. arXiv:1708.02002 [cs] (2018). <https://doi.org/10.48550/arXiv.1708.02002>
- [30] Sudre, C.H., Li, W., Vercauteren, T., Ourselin, S., Jorge Cardoso, M.: Generalised dice overlap as a deep learning loss function for highly unbalanced segmentations. In: Cardoso, M.J., Arbel, T., Carneiro, G., Syeda-Mahmood, T., Tavares, J.M.R.S., Moradi, M., Bradley, A., Greenspan, H., Papa, J.P., Madabhushi, A., Nascimento, J.C., Cardoso, J.S., Belagiannis, V., Lu, Z. (eds.) *Deep Learning in Medical Image Analysis and Multimodal Learning for Clinical Decision Support*, pp. 240–248. Springer, Cham (2017)
- [31] Rueden, C.T., Schindelin, J., Hiner, M.C., DeZonia, B.E., Walter, A.E., Arena, E.T., Eliceiri, K.W.: Imagej2: Imagej for the next generation of scientific image data. *BMC Bioinformatics* **18**, 529 (2017) <https://doi.org/10.1186/s12859-017-1934-z>
- [32] Beucher S, L.C.: Use of watersheds in contour detection. *International Workshop on Image Processing: Real-time Edge and Motion Detection/Estimation*, 12–21 (1979)
- [33] Tkachenko, M., Malyuk, M., Holmanyuk, A., Liubimov, N.: Label Studio: Data labeling software (2020-2025). <https://github.com/HumanSignal/label-studio>
- [34] This effect could be counteracted by adding a small random perturbation  $-0.01 < \epsilon < 0.01$  to every particle position that happens to be an integer. Together with rounding by floor, this would with a 50% probability change the position of those particles coming from the 'snapping region' to the next smaller integer. However, a better way to solve the problem

the are anti-aliased masks described in the next subsection.

- [35] Ester, M., Kriegel, H.-P., Sander, J., Xu, X.: A density-based algorithm for discovering clusters in large spatial databases with noise. In: Proceedings of the Second International Conference on Knowledge Discovery and Data Mining (KDD-96), pp. 226–231 (1996)
- [36] <https://creativecommons.org/licenses/by-sa/4.0/>